

# Understanding Systematic Errors Through Modeling of ALMA Primary Beams

Kara Kundert Urvashi Rau Edwin Bergin Sanjay Bhatnagar

**Abstract**—Many aspects of the Atacama Large Millimeter Array (ALMA) instrument are still unknown due to its young age. One such aspect is the true nature of the primary beam of each baseline, and how changes to the individual primary beams affect astronomical observations when said changes are ignored during imaging. This paper aims to create a more thorough understanding of the strengths and weaknesses of ALMA through realistic modeling of the primary beams and simulated observations, which in turn can inform the user of the necessity of implementing more computationally costly algorithms, such as A-Projection, and when simpler, quicker algorithms will suffice. We quantify our results by examining the dynamic range of each observation, along with the ability to reconstruct the Stokes I amplitude of the test sources. These tests conclude that for dynamic ranges of less than 1000, for point sources and sources much smaller than the main lobe of the primary beam, the accuracy of the primary beam model beyond the physical size of the aperture simply doesn't matter. In observations of large extended sources, deconvolution errors dominate the reconstructed images and the individual primary beam errors were indistinguishable from each other.

**Index Terms**—Aperture antennas, submillimeter wave propagation, radio interferometry, radio astronomy.

## I. INTRODUCTION

Radio interferometry has been a key innovation in the field of modern astronomy [1]. The ability to synchronize the observations of many separate antennas, along with dramatically improved bandwidths and backend technology, has led to increased observational sensitivities and precision in resolution. These improvements have led to the lowest systematic levels of noise ever seen in radio astronomy. As the technology used to create the digital backends of observatories continues to see astounding rates of progress, new sources of systematic errors that

were previously easily ignored are beginning to make their way above the ever falling noise floor. These newly unearthed sources of error have yet to be characterized and thoroughly understood, making them an especially treacherous threat for the astronomers using the observatories. This is even more prevalent in interferometric systems which combine numerous telescopes, often of different sizes, across a variable distance scale between antennas.

Though there are many factors contributing to each image, one that remains relatively unexplored is that of how the primary beam affects both the data collected and the final images produced [2]. As primary beams are related to the baseline apertures through a simple Fourier transform, the primary beam of each baseline offers a unique insight into the relative state of the antennas in an array. In this paper, we simulate several probable primary beam based systematic errors that could be introduced to the data collected at ALMA in order to better understand the effect it could have on the final images produced. These effects include but are not limited to improper calibration of the secondary reflector, minor offsets in the pointing during an actual observation, gravitational distortion of the aperture, and ignoring parallactic angle rotation during imaging. They also affect the final images in varying ways. For example, an offset of the receiver from the focus in the cryostat will change the way the aperture of the dish is illuminated, leading to phase errors and diminished signal amplitude. Finally, a pointing offset during observation produces phase errors and amplitude calibration issues dependent on the scale of the offset.

Without a thorough understanding of the health of the individual antennas and their relationships to each other while performing observations, new errors can proliferate into the images through incorrect calibration of

the primary beam in the imaging process. Such errors include but are not limited to the hiding of low-amplitude astronomical sources in the side lobes of brighter sources and an overall increase in the noise floor of an image relative to the baseline thermal noise.

Intrinsically, there are two questions to be answered about these revealed sources of error. What effects are they imparting on astronomical observations, and how can those effects be corrected? The work done on this simulation aims primarily to answer the first question. By creating a thorough and realistic model of ALMA, the simulation can observe the propagation of errors generated by selectively introducing perturbations to the primary beams. From this knowledge, software can be developed to target the largest sources of error in data analysis.

In the following section, the mathematics of the problem are summarized. In the subsequent two subsections, a brief description of the ALMA instrument and the experimental model is provided. This is followed by the results of our testing and the ramifications we predict for observations on the ALMA instrument.

## II. BACKGROUND

In the case of the ALMA and similar instruments, the visibility function of a source is observed and converted into images via a Fourier transform. As the interferometer is neither infinite in size nor sampling at every point in space, each visibility measurement becomes a discrete linear weighted sum of a range of spatial frequencies which are determined by the geometry of the instrument. This weighting is a function of the baseline apertures of the interferometer,  $A$ . The baseline aperture is found by correlating the aperture illumination functions of a pair of antennas in an array. This can be Fourier transformed to provide the primary beam,  $B$ . Both  $A$  and  $B$  determine how well a given baseline pair of antennas are able to see the true sky. In attempting to recreate the true image, the estimated primary beam of a given observation can be factored out in the final stages of data corrections and reduction, or used to correct the image using A-projection (an image processing algorithm further described in Section V) [3]. The better the estimated beam matches the true beam from the instrument, the better the corrections on the data will be. The main

question this simulation seeks to answer regards how much uncorrected changes in the primary beams of ALMA affect the final images produced using standard CLEAN tool, which is deconvolution and image correction software that operates by iteratively finding point-source peaks in an image and subtracting the scaled dirty beam (also called the point-spread function<sup>1</sup>, or PSF) from that point [4]. This method helps to minimize the effects of the sidelobes of the PSF and to make a true map of the point sources' locations and their amplitudes. There is also a version of CLEAN which enables the user to choose model sources of multiple sizes for larger objects. This tool is called MS-CLEAN [5].

First, the mathematical relationship between the observed visibilities and the sky brightness must be defined, along with how baseline apertures and primary beams can affect these observations. In its most basic form, for one timestep, baseline, and polarization, we get this Fourier pair of equations:

$$V_{obs} = V_{true} * A \quad (1)$$

$$I_{obs} = I_{true} \times B \quad (2)$$

where  $V_{obs}$  is the observed visibility,  $V_{true}$  is the true visibility,  $I_{obs}$  is the observed image,  $I_{true}$  is the true image. Note that  $*$  denotes the convolution function, and  $\times$  is multiplication. For a source defined on the celestial sphere, the Fourier relationship between the visibility function and the image is given by the van-Cittert-Zernike theorem, given in symbolic form in Eq. (3) [6].

$$V(u, v) \stackrel{\mathcal{F}}{\rightleftharpoons} I(l, m) \quad (3)$$

Now let us build further complexity into equation (1) by accounting for the geometry of the array, which we will mathematically describe as the sampling function  $S(u, v)$ .

$$V_{obs}(u, v) = [V_{true}(u, v) * A(u, v)] \times S(u, v) \quad (4)$$

where the sampling function  $S$  can be written as:

<sup>1</sup>Also sometimes referred to as the impulse response function.

$$S(u, v) = \sum_k \delta(u - u_k) \delta(v - v_k) \quad (5)$$

where each  $k$  represents a measurement from a single baseline.

Now finally, let us invert equation (4) via Eq. (3) to yield an image of the observed source brightness distribution, giving us a more complex and realistic version of Eq. (2).

$$I_{obs}(l, m) = [I_{true}(l, m) \times B(l, m)] * I_{psf}(l, m) \quad (6)$$

where  $I_{psf}$  is the Fourier transform of the sampling function  $S(u, v)$ .

In these equations for the simplified case of a single snapshot in a single frequency bin and a single baseline, we find that the observed image is the true sky multiplied by the primary beam and then convolved with the point-spread function. This is the mathematical foundation of the simulation.

#### A. The ALMA Observatory

In the case of ALMA, the array is still in its early science phase, so some parameters are bound to change as the remaining components of the instrument gradually come online. In its final design, ALMA will consist of a 12-m array composed of 50 antennas of two designs denoted as DA and DV with baselines ranging from 15m to 16km, a 12-element compact 7-m array with baselines ranging from 8.5m to 30m, and four 12-m antennas for single dish (or Total Power) observations, which provide spatial information equivalent to baselines of 0m to 12m. The 7-m and total power arrays – with their overall shorter baselines – aim to fill the hole in  $uv$ -coverage typically seen in radio interferometers. ALMA will be capable of observing from 31-950 GHz with full linear polarization (X, Y) [7].

However, ALMA is not yet fully finished. In Early Science Cycle 2 - which the simulation aims to model - the array has the following specifications: 34 12-m antennas of three separate designs, along with the Atacama Compact Array (ACA), which consists of nine identical

7-m dishes [8]. There are also two 12-m antennas in the Total Power Array, used to make single dish observations in order to fill the central hole in the  $u$ - $v$  plane. Each antenna is equipped with receivers to observe at bands 3, 4, 6, 7, 8, and 9, which corresponds to wavelengths of about 3.1, 2.1, 1.3, 0.87, 0.74, and 0.44 mm. There are many configurations of the array, with maximum baselines ranging from approximately 160 m to 1.5 km, though the maximum baseline for bands 8 and 9 is approximately 1 km.

One fact is evidently clear - ALMA is the foremost leader in interferometric imaging at millimeter wavelengths. As image fidelity is most strictly limited by the number and coverage of samples in the  $u$ - $v$  plane [9], the sheer number of antennas along with the variation in baseline spacings gives ALMA superior imaging capabilities to any other modern interferometer currently online. This unprecedented ability means that errors generated by systematic errors in primary beam analysis can limit the imaging capabilities of ALMA.

#### B. The Model

Our goal is to model a realistic interferometric array, with as many of the known problems of the ALMA primary beam as we know how to replicate computationally. In its most basic form, the simulation does the calculations shown in Eq. (4) for a set of mutually unique aperture models over a series of time steps. As time progresses in the simulation, so does the relative geometry of the array to the celestial sphere. An individual simulation is composed of snapshots taken every 3 minutes over the course of 2 hours, for a total of 40 snapshots per “observation”. Snapshots were chosen over integrations to conserve computational resources, the duration was chosen to prevent shadowing of closely-placed antennas.

The simulation is designed to be a test of the capabilities of ALMA in Cycle 2 of its early science testing. Therefore, the unperturbed interferometer which acts as the control case of the simulation has 34 identical apertures, taking data at 100 GHz in receiver band 3. The numerical interferometer is built by generating a set of antennas in an array, using the specifications on Cycle 2 released by ALMA, including the reference location of the observatory on the earth, the placements of the antennas

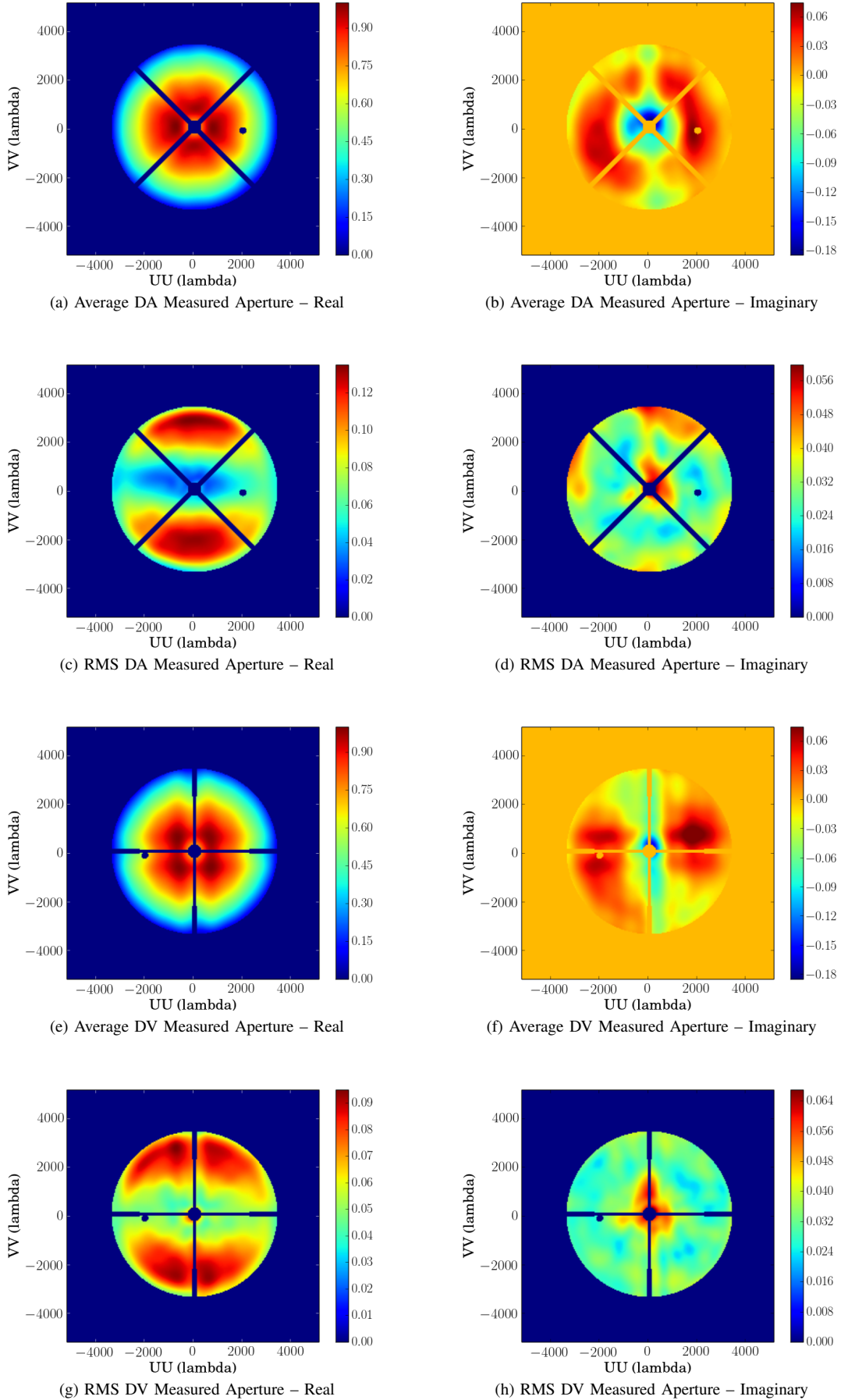


Fig. 1. The average real and imaginary components of the 12m DA- and DV-type apertures, pictured with the RMS variation between apertures, normalized by the maximum real response. While these apertures are based on true measurements of the aperture illumination, they neglect the effects of support leg diffraction.

in 3D space, the Stokes parameters, the rest frequency of the array, and its frequency resolution [8]. In this simulation, the minimum baseline between antennas is approximately 15 m and the maximum is approximately 800 m.

In choosing the perturbation effects to study, two sets of simulations were performed. The first was a preliminary, exploratory version and a variety of apertures, both simulated and measured, with handmade perturbations that included blind and corrected pointing offsets, ellipticity, noise on the aperture, parallactic angle rotation, and the uncorrected combination of the DA/DV antenna types (which have a  $45^\circ$  offset of the support legs). Several combinations of the above effects were also tested, in order to better understand how the perturbations compound with each other. These tests concluded that pointing offsets and illumination offsets were the dominant source of imaging errors. A more thorough description of the layout of this version and its results can be found in Appendix A.

The second version of the simulation (whose results are the focus of this paper) used solely measured apertures similar to the average ones shown in Fig. 1, and focused only on the strongest perturbation effects that were found in the previous round of testing. The pointing offset case used identical apertures modified only by the offset itself. The illumination offset case included a whole set of different apertures to test the effect of the variations depicted in Fig. 1. Parallactic angle rotation was ignored because it was found to be a relatively small effect similar to combining the DA and DV antennas for this short time range as can be seen in Table I, and because it is very computationally expensive to run. Polarization was also largely ignored for the sake of time.

Neglecting to correct for heterogeneous antenna combinations, such as using the ALMA Compact Array (ACA) with the 12-m array elements or varying designs of the 12-m antennas, was also chosen as a subject for investigation in both versions of the simulation. We have elected to include these results in order to both validate the results of our simulation, particularly in reference to previous work done on the CARMA instrument, and to understand and probe the relative differences between errors due to various effects within the simulation framework and improper handling of the

heterogeneous quality of the array [2].

By convolving the perturbed apertures, baseline aperture functions are calculated for each pair of antennas, the Fourier transform of which gives the primary beam of that baseline. For each baseline, the real component of this primary beam is multiplied by the true sky image. Visibilities were calculated from the perturbed data to produce a simulated data set using Eq. (4). The standard CASA<sup>2</sup> MS-CLEAN task is then run on these images of the “observed sky”. The off-source rms-level of the image is saved to disk. Image fidelity is also tested by finding the amplitude of the cleaned source divided by the normalized amplitude value of the CASA model primary beam at that point. This test was done to see how closely the primary beams need to match in order to get desired fidelity in image reconstruction.

Three main tests were run, a 1 Jy point source pointed slightly off-center, a small extended source (to emulate a protoplanetary disk or small cloud), and a large extended source to fill the whole primary beam, as can be seen in Fig. 2. The source in the point source test was located at approximate the 75% power point in the main lobe of an unperturbed primary beam. The small extended source was centered at approximately the 60% power level of the main lobe of the unperturbed primary beam. The large extended source was centered.<sup>3</sup> The simulated uv-coverage and antenna placement can be seen in Figure 3.

### III. RESULTS

Table II shows that the most prominent primary beam effects in this study were those involving pointing offsets. To prevent the introduction of pointing offset errors, ALMA creates pointing models for each antenna in the array. This is done in two ways. On a weekly basis, a short pointing run is made, conducted with 30-50 sources spread evenly between 20-85° elevation. This enables the array to “blindly” find any source in the sky with an accuracy between 2-4” [10]. Beyond that, in order

<sup>2</sup>Common Astronomy Software Application

<sup>3</sup>The small sources were placed off-center in order to observe the effects of primary beam corrections. A point source or small source that is perfectly or nearly perfectly centered in the beam would lead to only very small corrections from the primary beam, as it would be located at nearly maximum power. Primary beam correction errors are generated in the lower-power regions and side lobes of the image.

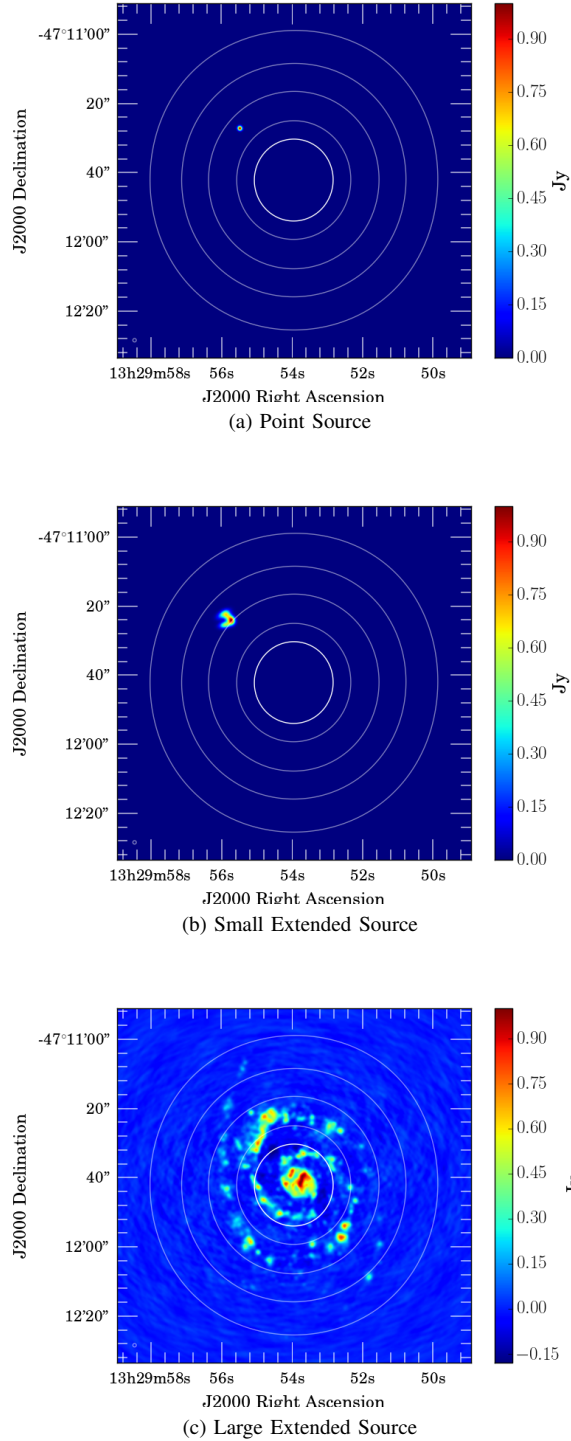


Fig. 2. The simulated sources used for each test. These are the point source (Fig. 2a), the small extended source (Fig. 2b), and the large extended source (Fig. 2c). The smaller sources are offset from the center of the image in order to introduce primary beam effects to the image, as a small centered source will not experience primary beam related perturbations. Also shown in each image are contours of the main lobe of the primary beam, drawn at 80%, 60%, 40%, and 20% power. The innermost contour indicates the largest image scale that the simulation is sensitive to, as set by the minimum uv-spacing.

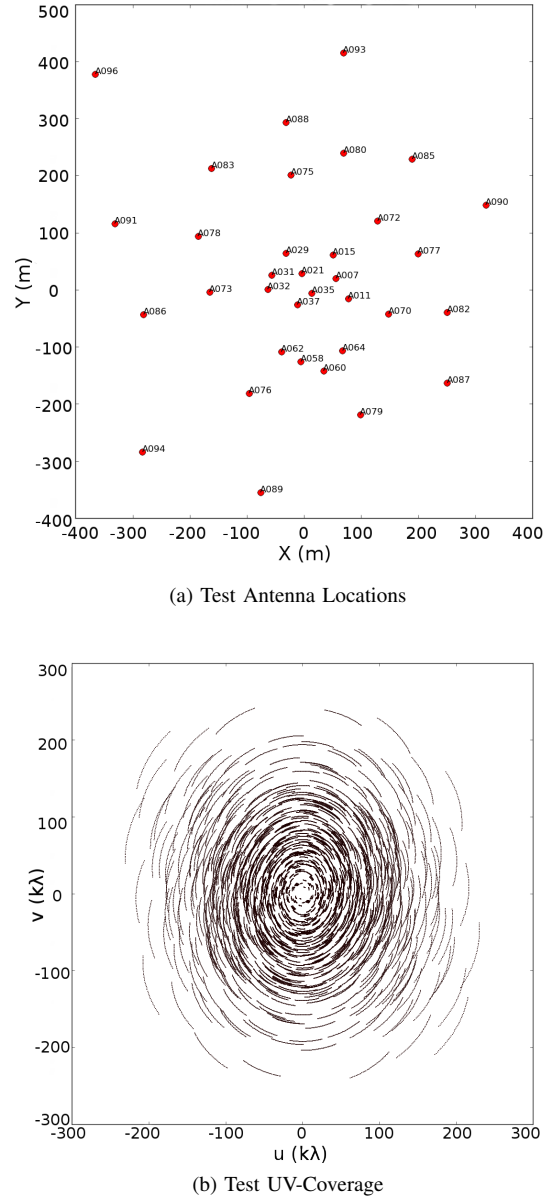


Fig. 3. The locations of the 34 antenna array used in all simulations in the experiment (Fig. 3a), and the uv-coverage generated from each observation (Fig. 3b). A hole in the center of the uv-field is clearly seen, as the compact array geometry was not included in the simulation.

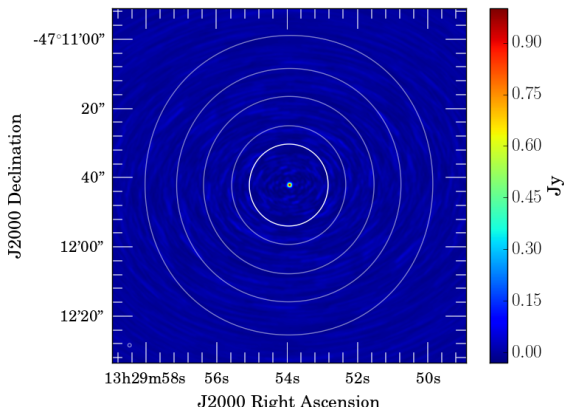


Fig. 4. The point-spread function (PSF) of the synthesized beam used in all tests, overlaid with contours of the main lobe of the primary beam at 80%, 60%, 40%, and 20% power. Tests were run with an array of 34 antennas, observing 40 snapshots over the course of 2 hours.

to ensure that an observed source can be held stable at the center of the beam, each scientific observation is preceded by an offset pointing which enables the array to track any source to within a Gaussian RMS of  $0.6''$  of its true position [10]. We refer to this case as a “corrected pointing offset”. While these seem like very high accuracies, these numbers are a reflection of telescope geometry, which makes them frequency invariant. Given the primary beam’s scaling with frequency, this means that the imaging effect of pointing errors will get progressively worse at higher frequencies – a corrected pointing offset at 400 GHz (or the middle of the range of ALMA’s observing capabilities) could be just as bad as a blind pointing at 100 GHz, the lowest band simulated here. As such, the numbers presented for blind pointing offsets at 100 GHz can also be considered a test of corrected pointing offsets at 400-800 GHz, which is a relevant case to a typical ALMA observer.

Simulated observations took place at 100 GHz, giving the primary beam a FWHM of approximately 45 arcseconds. At worst, the blind pointing offsets could shift the beam by almost 10% of its width. Tests for this case gave dynamic ranges of approximately 1000 for both the point source and small extended source cases. Numbers were also given for ALMA’s ability to self-correct for pointing offsets, which have a maximum of 0.5 arcseconds [7]. In the best case of corrected pointing

offsets for a 100 GHz observation, dynamic ranges were found to be approximately 4750 for the point source case and 3850 for a small extended source, or approximately 21 – 25% of the blind pointing offset case.

Illumination offsets, which occur when the optical access on the cryostat offsets the collected light slightly from the receiver, fell shortly below blind pointing offsets and slightly above the corrected pointing offset case, with a dynamic range near 3500 in the point source case and 2150 for the small extended source, or between approximately 29–47% the strength of the blind pointing offset case.

Results from the small extended source case indicate generally the same trend in the hierarchy of perturbation of data, though at slightly higher noise levels in all cases. Results from the large extended source are almost entirely flat, indicating that deconvolution errors are dominating over the problems in the primary beam.

However, the largest error came from changing the antenna sizes, with dynamic ranges from the source peak to the noise floor of around 300 in the single point source test and 175 in the small extended source test. This kind of data error would be generated by using the ALMA 7m and 12m arrays in conjunction with each other, with the small baselines of the 7m array filling in the center of the uv-coverage plane, without correcting for the use of three different combinations of antenna pairs leading to three different types of primary beams. This matched the expectations set up by previous work performed by Stuart Corder on the CARMA instrument, which found that even an uncorrected beam size differential of 3% would result in reduction in image fidelity by a factor of two [2].

A set of preliminary tests took place in 2013 to determine which perturbations merited more thorough investigation. These tests investigated a much broader selection of perturbation effects with less precision - the simulation used an array of only 10 antennas and 4 time steps over a simulated two-hour observation. Tests were run on point source observations, with one point source and one multi-source test per perturbation effect. The inverse dynamic ranges for these tests are given in Table I.

RMS-levels for the 34 antenna test case can be found in Table II, which we have defined as being the noise

floor of the simulated observation. As the peak amplitude was normalized to 1.0 Jy, these numbers also indicate the inverse dynamic range in each case.

#### IV. CONCLUSIONS

Initial results show that understanding the primary beam and how it affects observations is critical to the science being done at these instruments. The strongest effect in the simulation was found to be blind pointing offsets, with dynamic range from source peak to noise floor limited to less than 1000 in the test case of a single 2 hour observation of a point source. The next largest effects were illumination offsets and corrected pointing offsets, with dynamic ranges limited to less than 5000 in the best cases. Preliminary testing done in 2013 indicated that other varieties of primary beam perturbations, e.g. beam rotation, ellipticity, combination of the three kinds of 12m antennas, were relatively minor effects, with dynamic ranges at the 10,000 level or higher for a single point source observation.

The first effect to be concerned about would be the case of blind pointing offsets and high frequency corrected pointing offsets. At low frequencies, ensuring that all observations are done with use of pointing correction would certainly help. However, observations above 400 GHz are liable to see these same limits even with the help of the pointing guides, as pointing offsets have an effect that is relative to the size of the beam. As frequency goes up and the beam size shrinks, even a corrected pointing offset could have severe consequences on image quality. Previous work from the MMA as described in ALMA Memo #95 could potentially help to mitigate the effects of pointing errors, though only in the case of pointing errors that are known [11]. Since most cases of pointing offsets are random and hence difficult to characterize, this algorithm will likely do little to mitigate the effects of pointing offsets. However, an algorithm such as the Pointing SelfCal algorithm, which attempts to solve for the unknown pointing errors and incorporate those into the aperture illumination models to be used in the A-Projection algorithm during imaging, could potentially drastically reduce the magnitude of the errors propagated into final images through pointing offsets [5]. However, this algorithm has only been tested for images with much lower frequencies, so it is unclear how beneficial they

will be to the high frequency demands of ALMA. If a method could be devised to correct pointing offsets at the time of observation to the 0.01 – 0.05 arcsecond level, even the highest frequencies would retain dynamic ranges of 10,000 or higher.

With all other contributors having much smaller effects on the residuals in standard imaging procedures, effort should be directed towards correcting for these larger effects before they start seriously impeding the scientific goals of the ALMA instrument. Efforts should also be made to improve deconvolution algorithms, in order to improve imaging of extended objects to the point that primary beam perturbations can begin to affect the data.

Finally, the lack of proper calibration and clean-up of mixed-array data was found to be a disastrous source of excess image noise, limiting the image dynamic range to less than 300 in the best case of an unresolved point source over one 2-hour observation. This was the expected result which affirmed the accuracy of our ALMA model relative to previous similar tests done at CARMA [2]. The 7m and 12m arrays are designed to be used together, with the 7m array filling in the uv-coverage hole that couldn't be filled with the larger 12m dishes. If the algorithms and software used for full-beam imaging do not account for the valid physical differences in the apertures (and hence their primary beams), our testing indicates a starkly limited dynamic range on observations. This kind of algorithm is already available in the ALMA Science Pipeline, and therefore shouldn't affect further imaging efforts.

##### A. Notes for ALMA Users

These tests aimed to quantify the dynamic ranges at which different errors begin to affect the quality of ALMA images when left ignored during the imaging process. This information is useful to decide when one needs to invoke computationally expensive algorithms, such as A-Projection, when simpler methods and algorithms will clean data without sacrificing image quality.

Taking the full complexity of ALMA beams into account via A-Projection is computationally expensive because with  $N$  different apertures, there are  $N(N-1)/2$  separate primary beams (one per unique baseline), each of which has to be precomputed and cached at different parallactic



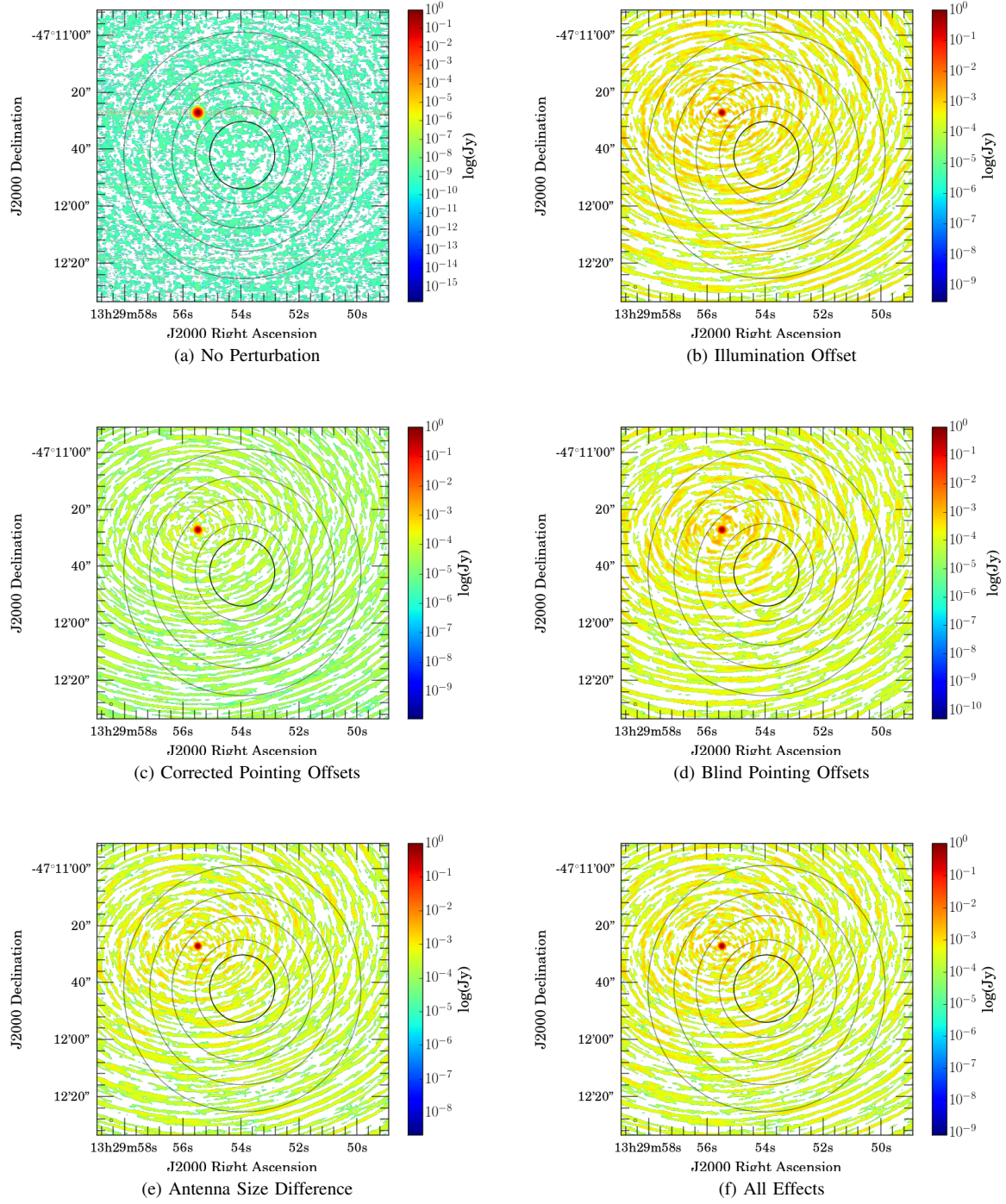


Fig. 5. These images show the progression in overall noise as related to the perturbing effects, corresponding to successive rows in Table II. All images were saturated to the same level in order to make the background noise visible.

angles. Taking the example of the final, full ALMA array (with 66 antennas) and sky rotations calculated at  $5^\circ$  increments, over 25,000 separate convolution functions would have to be calculated over a 4 hour observation. Computing one baseline beam and rotating it incurs errors, so each one must be computed separately. The  $uv$ -resolution at which this must be calculated also depends on the particular setup of an individual imaging run. All in all, it is clear that it is of immense practical value to understand precisely when this full detail is needed and when various approximations will suffice.

Our results provide the following guidelines: for dynamic ranges of less than 1000, the accuracy of the primary beam model (beyond physical aperture size) simply does not matter. At dynamic ranges beyond 1000, pointing offsets will begin to affect final image quality, followed by changes in beam shape due to illumination offsets beyond dynamic ranges of 5000. Finally, parallactic angle rotation and the beam differences between the DA/DV antennas will become appreciable at dynamic ranges beyond 10,000.

## V. FUTURE WORK

Future tests could investigate the benefits of A-projection in image correction [3]. A-projection uses a model of the aperture in the initial steps of imaging and deconvolution in order to remove its effects from the final image. The idea goes that the baseline apertures  $A$  have contributed various effects into the visibilities as they are observed, as described in (1). In order to remove those effects, the observed visibilities must be convolved with the inverse of the baseline aperture function  $A^{-1}$ , as seen in (7). The baseline aperture and its inverse will then form a unity matrix, returning the true visibilities, which can be Fourier transformed into the true image.

$$V_{true} = A^{-1} * V_{obs} \quad (7)$$

$$A^{-1} = \frac{A^\dagger}{AA^\dagger} \quad (8)$$

This process takes place during the regridding of the visibilities, so that  $A^{-1}$  replaces the weighting function that evenly samples the  $u$ - $v$  plane. However,  $AA^\dagger$  may contain zero valued components. As such, formal division

by  $AA^\dagger$  is an extremely dangerous computation to make, as it has the potential to fill the  $u$ - $v$  plane with divide-by-zero errors and create an entirely erroneous image. Instead, the Fourier transform relationship between the aperture and the primary beam is used to rewrite (7) and (8) as

$$V_{cor} = A^\dagger * V_{obs} \quad (9)$$

$$B^2 \stackrel{\mathcal{F}}{=} AA^\dagger \quad (10)$$

$B^2$  is later factored out of the final image to recover  $I_{true}$ , minimizing the divide-by-zero errors while maintaining the integrity of the A-projection relationship. This method allows for a great deal of instrumental image correction prior to actually entering the image domain, assuming an accurate model of the aperture functions  $A$  is used.

Another subject for further exploration would be the utilization of the full complex beam in imaging in order to better understand the propagation of primary beam errors through the Stokes polarization planes, such as the effect of beam squint, which would appear in the Stokes Q plane in ALMA data. While our simulation used the full complex apertures to construct complex beams, only the real component of the primary beam was used in imaging as we were focusing solely on the Stokes I plane. Furthermore, the complicated complex structure of the aperture functions and their significant antenna-to-antenna variations (as seen in the real and imaginary RMS apertures presented in Fig. 1) will lead to residual phase structure in the complex primary beam which will affect Stokes I imaging as well.

Since the computational cost of A-Projection increases significantly if antenna-to-antenna variation is included, it is of interest to determine tolerance levels at which, if correctable in the hardware, antenna-to-antenna variations may be ignored up to some high dynamic range. In the results presented in this study, the effect of aperture illumination offsets on the real part of the primary beam is already the most significant factor beyond uncorrected pointing offsets and neglecting to correct for heterogeneous array elements. The effects of aperture illumination are likely to become more significant when the residual phase structures in the beams are also

included. Further studies will evaluate the significance of this effect.

Finally, a version of this simulation performed with full high-resolution measured apertures, including antenna arm diffraction, could also provide helpful information to ALMA users. So far no such testing has taken place for lack of such apertures.

## VI. ACKNOWLEDGEMENTS

It brings the authors great pleasure to thank Ken Kundert, Rick Perley, and Tom Rice for useful discussions. This work was supported in part by the National Radio Astronomy Observatory's Summer Student Research Assistantship Program.

## REFERENCES

- [1] G. W. Swenson, Jr. and N. C. Mathur, "The interferometer in radio astronomy," in *Proceedings of the IEEE*, vol. 56, December 1968.
- [2] S. A. Corder, "Optimizing image fidelity with arrays," Ph.D. dissertation, California Institute of Technology, 2009.
- [3] S. Bhatnagar, T. J. Cornwell, K. Golap, and J. M. Uson, "Correcting direction-dependent gains in the deconvolution of radio interferometric images," *Astronomy & Astrophysics*, vol. 487, no. 1, pp. 419–429, 2008.
- [4] J. A. Högbom, "Aperture synthesis with a non-regular distribution of interferometer baselines," *Astronomy & Astrophysics Supplement*, vol. 15, pp. 417–426, 1974.
- [5] S. Bhatnagar, "Calibration and imaging challenges at low radio frequencies: An overview of the state of the art," in *The Low-Frequency Radio Universe*, ser. ASP Conference Series, vol. LFRU, June 2009.
- [6] A. R. Thompson, J. M. Moran, and G. M. Swenson, Jr., *Interferometry and Synthesis in Radio Astronomy*. John Wiley & Sons, Inc., 1986.
- [7] A. Lundgren, *ALMA Cycle 2 Technical Handbook*, 1st ed., ALMA, 2013.
- [8] ALMA, *Cycle 2 Capabilities*, ALMA, 2013.
- [9] M. C. H. Wright, "Image fidelity," Berkeley Illinois Maryland Association, Memo 73, 1999.
- [10] T. van Kempen, S. Corder, R. Lucas, and R. Mauersberger, "How alma is calibrated: I. antenna-based pointing, focus and amplitude calibration," in *ALMA Newsletter*, ser. ALMA in-depth. ALMA Observatory, February 2012, no. 9, pp. 8–16.
- [11] M. A. Holdaway, "Imaging with known pointing errors," Millimeter Array, Memo 95, 1993.

## APPENDIX A PRELIMINARY RESULTS

Preliminary tests were performed over the summer and fall of 2013, focusing mainly on building a functioning architecture upon which further, more realistic tests could later be performed. As such, the main structure of the model is the same as described in Section II-B: a numerical array is constructed by generating a set of apertures in an array, those apertures are converted into primary beams based on their location and perturbation information, these primary beams are multiplied by the true sky image to create an “observed sky”, and CLEAN is run on these images. Statistics are then measured off of these images, such as the rms-noise level, dynamic range of the peak-to-noise, and the image fidelity.

In this preliminary testing period, the parameters for testing were chosen in an effort to minimize testing time while still getting useful results for a wide range of aperture types and perturbation effects. As such, the simulation was run with 10 antennas taking 4 snapshots over a two-hour “observation”. Two main tests were run, a single point source test and a multi-source test with four point sources. The sources were placed at various points in the main lobe of the primary beam (75%, 60%, and 30% power points of the PB), with the fourth source located in the first side lobe. The source in the single source case was located at approximately the 85% power point of the main lobe. This was done in an attempt to investigate how the side lobes of the primary beam change with perturbations, the effects of which are expected to be much different than in the main lobe.

This overall computational minimization allowed us to factor in full time-dependence, including parallactic angle rotation. We also tested a variety of types of apertures of varying scales of realism. In the most basic test, there was a script in the simulation to generate a Numeric Python (NumPy) array containing the array. In this case, the array was completely flat and real, and contained very little of the more interesting and realistic structures of the other tested apertures. Tests were also run using two kinds of ray-traced aperture models - one made in CASA using the ALMA parameters, and one made by Dr. Stuartt Corder with an imposed feed-leg shadow mask excluding diffraction effects through data taken in holography measurements. While both the CASA ray-traced apertures and the measured apertures are clearly much more realistic than the Python-generated apertures, only the measured apertures include imaginary structure, making them the only ones to enable Stokes polarization analysis<sup>4</sup>.

Below is a table displaying the inverse dynamic ranges for each of the tests performed, where the inverse dynamic range is defined as the rms-noise power level of the image divided by the peak source power level. We tested the effects of size differences in the apertures (denoted as 7m, 12m in the table), parallactic angle rotation of the beams, change in the orientation of the beams (to model the difference between the DA/(DV/PM)<sup>5</sup> antenna types in ALMA, one of which has support legs that have been rotated by 45° relative to the other), blind and corrected pointing offsets, and illumination offsets of the beams. We also tested various combinations of these effects, which can be found in the tables below. We were only able to test size difference effects using the NumPy-generated beams as we hadn’t been able to acquire measured or CASA-ray traced apertures for the 7m antennas. We were also only able to perform illumination offset tests on the measured beams, as they were the only apertures that had illumination information.

<sup>4</sup>Note that while there was some initial investigation done of primary beam effects and polarization, this was eventually set aside before the version of the simulation detailed in this paper. As such, only the real component of the beam was used in image calculations.

<sup>5</sup>The DV and PM models of antenna are very similar to each other in design, so any differences in their primary beam are expected to have essentially undetectable effects on imaging. However, the PM model antenna is only used in the Total Power Array.

TABLE I  
APPROXIMATE INVERSE DYNAMIC RANGE LEVELS FOUND IN THE CORRECTED IMAGES OF THE PRELIMINARY RUNS OF THE SIMULATION,  
USING 10 ANTENNAS AND 4 TIME STEPS.

|   | Single Source         | Multi-Source          |
|---|-----------------------|-----------------------|
| 7m, 12m, NumPy-Generated  | $4.55 \times 10^{-5}$ | $2.86 \times 10^{-4}$ |
| Unperturbed, NumPy-Generated  | $3.17 \times 10^{-9}$ | $2.99 \times 10^{-9}$ |
| Parallactic Angle Rotation, NumPy-Generated                                 | $6.74 \times 10^{-7}$ | $1.84 \times 10^{-5}$ |
| DA/DV, NumPy-Generated  | $3.91 \times 10^{-6}$ | $3.89 \times 10^{-5}$ |
| DA/DV with Parallactic Angle Rotation, NumPy-Generated                      | $3.99 \times 10^{-6}$ | $4.23 \times 10^{-5}$ |
| Blind Pointing Offsets, NumPy-Generated                                     | $2.85 \times 10^{-5}$ | $6.18 \times 10^{-5}$ |
| Corrected Pointing Offsets, NumPy-Generated                                 | $7.82 \times 10^{-6}$ | $1.69 \times 10^{-5}$ |
| Corrected Pointing Offsets with Parallactic Angle Rotation, NumPy-Generated | $4.78 \times 10^{-6}$ | $2.74 \times 10^{-5}$ |
| DA/DV with Corrected Pointing Offsets, NumPy-Generated                      | $5.39 \times 10^{-6}$ | $5.84 \times 10^{-4}$ |
| Unperturbed, CASA Ray-Traced  | $3.19 \times 10^{-9}$ | $3.60 \times 10^{-9}$ |
| Parallactic Angle Rotation, CASA Ray-Traced                                 | $8.52 \times 10^{-7}$ | $1.32 \times 10^{-5}$ |
| DA/DV, CASA Ray-Traced  | $3.42 \times 10^{-7}$ | $4.53 \times 10^{-6}$ |
| DA/DV with Parallactic Angle Rotation, CASA Ray-Traced                      | $8.52 \times 10^{-7}$ | $1.32 \times 10^{-5}$ |
| Blind Pointing Offsets, CASA Ray-Traced                                     | $2.29 \times 10^{-5}$ | $4.81 \times 10^{-5}$ |
| Corrected Pointing Offsets, CASA Ray-Traced                                 | $6.19 \times 10^{-6}$ | $1.98 \times 10^{-5}$ |
| Corrected Pointing Offsets with Parallactic Angle Rotation, CASA Ray-Traced | $7.28 \times 10^{-6}$ | $2.20 \times 10^{-5}$ |
| DA/DV with Corrected Pointing Offsets, CASA Ray-Traced                      | $5.32 \times 10^{-6}$ | $1.54 \times 10^{-5}$ |
| Unperturbed, Measured   | $4.47 \times 10^{-9}$ | $7.76 \times 10^{-9}$ |
| Parallactic Angle Rotation, Measured  | $4.05 \times 10^{-6}$ | $2.48 \times 10^{-5}$ |
| DA/DV, Measured   | $3.13 \times 10^{-6}$ | $2.84 \times 10^{-5}$ |
| DA/DV with Parallactic Angle Rotation, Measured                             | $5.83 \times 10^{-6}$ | $2.78 \times 10^{-5}$ |
| Blind Pointing Offsets, Measured  | $1.27 \times 10^{-5}$ | $5.90 \times 10^{-5}$ |
| Corrected Pointing Offsets, Measured  | $4.70 \times 10^{-6}$ | $1.33 \times 10^{-5}$ |
| Corrected Pointing Offsets with Parallactic Angle Rotation, Measured        | $8.78 \times 10^{-6}$ | $2.93 \times 10^{-5}$ |
| DA/DV with Corrected Pointing Offsets, Measured                             | $2.49 \times 10^{-5}$ | $6.28 \times 10^{-5}$ |
| Illumination Offsets, Measured  | $8.85 \times 10^{-5}$ | $2.46 \times 10^{-5}$ |

## APPENDIX B FULL MODEL RESULTS

TABLE II  
APPROXIMATE INVERSE DYNAMIC RANGE LEVELS FOUND IN THE CORRECTED IMAGES OF THE FULL SIMULATION, USING 34 ANTENNAS  
AND 40 TIME STEPS. ALL TESTS USED MEASURED APERTURES. THE "ALL EFFECTS" CASE INCLUDES CORRECTED POINTING OFFSETS,  
ILLUMINATION OFFSETS, AND SIZE DIFFERENCE PERTURBATIONS IN THE PRIMARY BEAMS USED IN THE IMAGING PROCESS.

|                            | Point Source         | Small Extended Source (Off-Center) | Large Extended Source |
|----------------------------|----------------------|------------------------------------|-----------------------|
| No Perturbation            | $6.0 \times 10^{-8}$ | $7.6 \times 10^{-5}$               | 0.013                 |
| Corrected Pointing Offsets | $2.1 \times 10^{-4}$ | $2.6 \times 10^{-4}$               | 0.013                 |
| Illumination Offsets       | $2.8 \times 10^{-4}$ | $4.6 \times 10^{-4}$               | 0.013                 |
| Blind Pointing Offsets     | $1.0 \times 10^{-3}$ | $9.6 \times 10^{-4}$               | 0.013                 |
| Size Difference            | $3.3 \times 10^{-3}$ | $5.7 \times 10^{-3}$               | 0.014                 |
| All Effects                | $3.5 \times 10^{-3}$ | $6.1 \times 10^{-3}$               | 0.014                 |